Chemical Engineering & Processing: Process Intensification 158 (2020) 108203

Contents lists available at ScienceDirect

Chemical Engineering and Processing - Process Intensification

journal homepage: www.elsevier.com/locate/cep

Numerical analysis of the hydrodynamics induced by rotating ring electrode using κ-ε models

Juan A. Yáñez-Varela [a], Israel González-Neria [a], Alejandro Alonzo-García [b], Gabriela Rivadeneyra-Romero [c], Sergio A. Martínez-Delgadillo [d,*]

[a] Posgrado en Ing. de Procesos, Universidad Autónoma Metropolitana Azcapotzalco, Av. San Pablo No. 180. Azcapotzalco, C.P. 02200, CDMX, Mexico
[b] CONACyT-Tecnológico Nacional de México, Instituto Tecnológico de Nuevo León, Centro de Investigación e Innovación Tecnológica. Av. de la Alianza No. 507, Parque de Investigación e Innovación Tecnológica, Apodaca, Nuevo León, CP 66629, Mexico
[c] Universidad del Istmo, Ingeniería de Petróleos, Ciudad Universitaria S/N, Barrio Santa Cruz 4ª Secc., Sto. Domingo, Tehuantepec, 70760, Oaxaca, Mexico
[d] Depto. Ciencias Básicas, Universidad Autónoma Metropolitana Azcapotzalco, Av. San Pablo 180. Azcapotzalco, C.P. 02200, CDMX, Mexico

ARTICLE INFO

Keywords:
Rotating ring electrode
κ-ε models
Fluid flow analysis
Electrochemical reactor

ABSTRACT

The dynamic rotating rings electrode (RRE) has proven to be an efficient configuration for removing contaminants. The flow induced by the complex geometry of the RRE was analyzed by computational fluid dynamics (CFD) and the multiple reference frame approach (MRF), rotational speed in the range of 75–500 rpm. Assessment of the three κ-ε type models (standard, renormalization group theory (RNG) and realizable) to solve the turbulent flow was performed. The results show that the realizable model provides a more adequate physical description of the flow than the other models. The global flow was analyzed using integral parameters such as the average flow, circulation time, pumping number, and power number. The local flow was examined qualitatively through velocity profiles and streamlines. The effect of simulating two different positions (0° and 45°) of the RRE moving walls concerning the baffles when using the MRF approach was evaluated. The flow pattern is predominantly radial because the electrode external bars propel the fluid to the lateral tank wall. Besides, the external bars promote regions of high deformation in the fluid that produce vortices. It was found that the result at 0° is in good agreement with the experimental results of mixing time.

1. Introduction

Nowadays, electrochemical processes such as electrocoagulation, electroflotation, and electroreduction are important alternatives in the treatment of liquid waste contaminated with organic and inorganic compounds. Different success stories have been well documented and reviewed by many authors, highlighting that the advantages of its flexible implementation and operation make it attractive to solve environmental problems on a real scale [1,2]. However, the high energy consumption remains a disadvantage in the profitability of this technology when treating wastewater. To improve energy performance, developers of environmental electrochemical technologies have chosen to intensify the reaction units. The application of magnetic fields, ultrasound (sonoelectrochemistry), and ultraviolet light (photoelectrochemistry) are some techniques in development to intensify electrochemical reactors [3].

A classic way to enhance the performance of electrochemical reactors is through improving their hydraulic behavior. Currently, the hydraulic improvement of electrochemical reactors is implemented through a rigorous design with modern tools such as computational fluid dynamics (CFD) [4]. These numerical tools allow solving the equations that govern the transport of momentum, mass, and energy in the domain of the fluid inside of the electrochemical reactor. The information from the numerical models is useful to improve the geometric detail of the reactor and allows establishing optimum operating conditions for each particular process. An approach adopted by different works is to analyze the flow in a single-phase, neglecting the effects of the gas generation that takes place in various electrochemical processes [5]. This assumption reduces the complexity of the phenomenological problem, saves computational costs of the simulation, and provides sufficient information to improve the hydraulic performance of the reactor. The classic parallel plate reactor is an example of the improvements that this approach can bring to the performance of electrochemical reactors. The numerical analysis allowed identifying the geometry of the manifold,

* Corresponding author.
E-mail address: samd@azc.uam.mx (S.A. Martínez-Delgadillo).

https://doi.org/10.1016/j.cep.2020.108203
Received 23 June 2020; Received in revised form 16 September 2020; Accepted 19 October 2020
Available online 27 October 2020

which has the function of distributing the electrolyte into the reactor at the inlet, as a key component [6]. Different arrangements have been proposed in the opening angle of the manifold, as well as different separations between the plates, to obtain better yields [7]. Another example is the extensive work by Choudhary et al. [8,9] on a continuous electrocoagulation reactor for textile wastewater treatment. They determined the best hydraulic operating conditions of the reactor (anode stirring speed and flow rate) using CFD analysis that was experimentally verified in the removal of color and chemical oxygen demand in wastewater.

The rotating rings electrode (RRE) has been widely applied to remove hexavalent chromium from the rinsing waters of the electroplating industry. With this electrode, the kinetic behavior of the process was studied in batch and continuous reactors [10]. The laboratory-scale results motivated the implementation of this configuration at a semi-industrial scale, where it was shown that it had low energy requirements [11]. To improve the performance of the reactor, the hydraulic behavior of the electrochemical reactor was analyzed using CFD. Flow variables such as turbulent intensity and vorticity were correlated to the experimental performance and conclude that the geometry of the RRE has a poor mixing inside the rings and limits its efficiency at high agitation velocities [12,13]. Based on the conclusion of the previous works, different tests, including internal bars and pitched blade impellers at the interior of the rings, to increase the pumping capacity of the axial flow of the electrode were performed [14]. These changes increased the axial flow, which improved mixing times.

As known, experimental techniques as particle image velocimetry (PIV) or laser doppler velocimetry (LDV) rely on translucent walls. This particular drawback limits the applicability to reactors with complex rotary systems such as the RRE as they interfere with both, the laser and camera. Therefore, this work aims to improve the knowledge about the flow behavior produced by the rotating rings electrode reactor by using CFD tool.

The κ-ε models in different conventional classical impellers geometries have been implemented, but there is a lack of knowledge about their performance with complex rotary systems as the RRE. In this work, the numerical analysis is performed by exploring three different RANS turbulence models, standard, RNG, and realizable to determine, which is the most appropriate to predict the flow patterns developed inside the reactor with rotating rings electrode. The comparison of the κ-ε models at 150 rpm was performed. The approach used to solve the movement of the electrode was the multiple reference frame (MRF) because it is economical in computational resources, and it is especially useful in studies, which rely on multiple runs. The hydrodynamics of the system with parameters classically used in the analysis of stirred tanks is analyzed, comparing the results obtained by simulating the steady-state flow in two alignment positions (0° and 45°) of the moving walls (electrode) concerning the static walls (baffles). In addition to the global analysis, the local behavior of different flow variables is inspected, which leads to the identification of possible improvements that can be implemented to the electrode geometry. The simulation with the experimental results of mixing time at the speed of 150 rpm is validated.

2. Methodology

2.1. Electrochemical reactor

The electrochemical reactor consists of a cylindrical tank with a 16 L capacity. The diameter of the tank (T) is 0.27 m and the height that the liquid reaches (H) is 0.295 m. The tank has four baffles with a width of $T/10$ to prevent vortex formation. The RRE consists of 14 rings with a diameter (D) of 0.14 m. Seven rings act as cathodes and seven as anodes connected in a monopolar manner using three flat external bars located outside the rings. Four internal bars that connect with the top two rings support the rings and the bottom two rings with two center shafts that connect to the direct current source and the variable speed motor (Fig. 1 A).

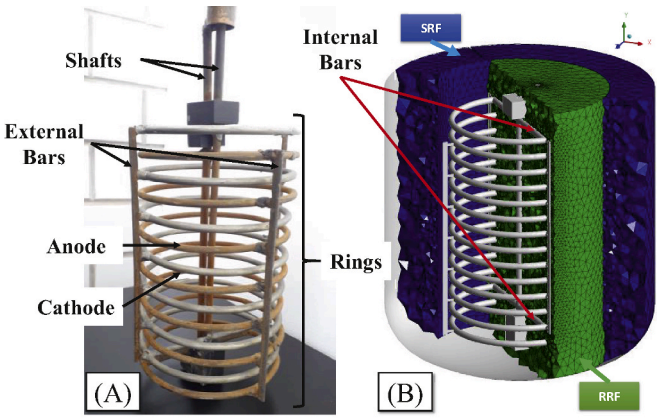

Fig. 1. (A) RRE photograph and (B) unstructured mesh of the computational domain.

2.2. Experimental measurements of mixing time

The tracer used in these tests was a KCl solution with a concentration of 250 g·L^{-1}. Ten mL of the solution into the reactor through a glass tube 0.01 m below the surface of the liquid to avoid the effects of the surface tension were injected. The conductivity change was recorded with the CONSORT C3010 multi-parameter equipment. Two probes were submerged 0.1 m below the surface of the liquid. The location of the probes was between baffles, 45° apart from each other. The conductivity probes used, allow a maximum delay in the measurement of 0.3 s. To avoid uncertainty due to this effect, the equipment was programmed to record data every 1 s. Fifteen experimental runs were carried out, verifying the calibration of the probes every three experiments. The recorded conductivity data were normalized and with them, the coefficient of variation was calculated, when it falls below 5%, that time is taken as the mixing time (θ95%).

2.3. Model equations

Since the problem in the entire computational domain is solved i.e., in all three dimensions, a system of four partial differential equations will be solved, three of them are the Navier-Stokes equations in each direction and the fourth is the equation of continuity. To know the flow regime of the electrochemical reactor, the Reynolds number (N_{Re}) defined for a stirring system Eq. (1) is used:

$$N_{Re} = \frac{\rho N D^2}{\mu} \tag{1}$$

where N is the angular velocity in s^{-1}, D is the electrode diameter in m, ρ, and μ, are the density and viscosity of water at 25 °C. Because the electrode is operated at speeds above 75 rpm ($N_{Re} > 10^4$), it is necessary to resolve the turbulent flow. In this work, the Navier-Stokes equations with the Reynolds Averaged Navier-Stokes (RANS) to approximate the turbulent flow is used. In this approach flow properties such as velocity (u) are replaced by the sum of the mean velocity (U) and the fluctuating component (u'). Using this approach and assuming incompressible flow, the continuity equation is defined as in Eq. (2):

$$\frac{\partial U_j}{\partial x_j} = 0 \tag{2}$$

While the moment equation turns out (Eq. (3)):

$$\frac{\partial}{\partial x_j}\left(U_i U_j\right) = -\frac{1}{\rho}\frac{\partial \overline{P}}{\partial x_j} + \frac{\partial}{\partial x_j}\left[\frac{\mu}{\rho}\left(\frac{\partial U_i}{\partial x_j} + \frac{\partial U_j}{\partial x_i} - \frac{2}{3}\delta_{ij}\frac{\partial U_i}{\partial x_i}\right)\right] + \frac{\partial}{\partial x_j}\left(-\rho\overline{u'_i u'_j}\right) \tag{3}$$

Where U is the mean velocity vector in $m{\cdot}s^{-1}$, x is the position vector in cartesian coordinates (i.e. x, y, and z) in m, $\overline{P}$ is the average pressure in Pa and δ_{ij} is the Kronecker delta. Writing the moment equation in the averaged form (Eq. (3)) the apparition of a new term $(-\rho\overline{u'_i u'_j})$, which accounts for the mean product of the velocity fluctuating motions. This term is known as the Reynolds stress term. The models of class "κ-ε" are models based on the Boussinesq hypothesis, where a new flow property is presented: the turbulent viscosity (μ_t), defined in Eq. (4).

$$\mu_t = \rho C_\mu \frac{\kappa^2}{\varepsilon} \tag{4}$$

This new property is a function of two variables that are the turbulent kinetic energy (κ), and the turbulent dissipation rate (ε). To model these two new variables, two conservation equations are defined for each property (Eqs. (5) and (6)).

$$\frac{\partial(\rho\kappa)}{\partial t} + \frac{\partial}{\partial x_i}(\rho U_i \kappa) = \frac{\partial}{\partial x_i}\left(\rho\frac{\upsilon_{eff}}{\sigma_\kappa}\frac{\partial \kappa}{\partial x_i}\right) + \rho(P_\kappa - \varepsilon) \tag{5}$$

$$\frac{\partial(\rho\varepsilon)}{\partial t} + \frac{\partial}{\partial x_i}(\rho U_i \varepsilon) = \frac{\partial}{\partial x_i}\left(\rho\frac{\upsilon_{eff}}{\sigma_\varepsilon}\frac{\partial \varepsilon}{\partial x_i}\right) + S_\varepsilon \tag{6}$$

The effective dynamic viscosity and effective kinematic viscosity considered by these equations are defined as $\mu_{eff} = \mu + \mu_t$ and $\nu_{eff} = \mu_{eff} / \rho$, respectively. In Eq. (6), P_κ represents turbulent kinetic energy production as a function of turbulent kinematic viscosity ($\nu_t = \mu_t / \rho$) according to Eq. (7):

$$P_\kappa = \nu_t\left(\frac{\partial U_i}{\partial x_j} + \frac{\partial U_j}{\partial x_i}\right)\frac{\partial U_i}{\partial x_j} \tag{7}$$

The generation term of Eq. (6) (S_ε) changes as a function of the type of the model "κ-ε" used, as well as the value of the empirical constants σ_κ, σ_ε, and $C\mu$. Table 1 shows the generation terms and the values of the constants used in this work for each κ-ε model. To simulate the mixing time, the non-reactive species transport equation is used (Eq. (8)).

$$\frac{\partial(\rho w_A)}{\partial t} + \frac{\partial}{\partial x_i}(\rho U_i w_A) = \frac{\partial}{\partial x_i}\left[\left(\rho D_A + \frac{\mu_t}{Sc_t}\right)\frac{\partial w_A}{\partial x_i}\right] \tag{8}$$

where; w_A is the mass fraction of the tracer, D_A is the diffusion coefficient, which in this work is given a value of $10^{-9}\,m^{-2}\,s^{-1}$, a typical value for liquids and Sc_t is the Schmidt turbulent number and in this work, it was set at a value of 0.7 to use the gradient diffusion hypothesis incorporated in Fluent®.

2.4. Numerical details of the solution

The numerical solution of the equations was carried out using the finite volume method with the commercial software Ansys Fluent®. To simulate the rotational movement of RRE, the multiple reference approach (MRF) was used. A region of the computational domain that surrounds the rotating walls (electrode) within a cylinder is defined (green zone in Fig. 1B), which is known as a rotational reference frame (RRF). In all the cells in the RRF, the angular speed is the one to be tested. The rest of the domain (blue zone in Fig. 1A) is considered as a static reference frame (SRF), so at the start of the simulation, the angular velocity is defined as zero. In the surface of the liquid, the inviscid wall was applied ($\tau = 0$), this is valid when using baffles, which greatly prevent the deformation of the liquid surface. For all the solid walls, the non-slip condition was defined, however, baffles and the tank wall were considered as static walls ($u = 0$), meanwhile, the electrode walls, were considered as moving walls with the velocity relative to the adjacent cell zone, that is, the velocity in the RRF. The treatment of the turbulent flow near solid walls was achieved using the "standard logarithmic wall functions" proposed by Launder & Spalding in 1974 [16]. The considerations made in this work at the solid walls of the model were used in many works dedicated to the study of the flow developed by stirred tanks [17]. This approach is useful since it is possible to capture velocity gradients developed on complex surfaces such as impellers, and it was shown that it has a good agreement with the experimental observations obtained with detailed methods e.g. LDV [18] or PIV [19].

The partial differential equations of the model are converted to algebraic equations through spatial discretization and solution schemes. To solve the set of algebraic equations the Semi-Implicit Pressure Linked Equations algorithm (SIMPLE scheme) was used. Second-order discretization schemes were used for all variables. To ensure that the solution is independent of the number of elements that the mesh contains, three meshes were built, additionally, to avoid false spatial convergence, the grid sizes were sequentially doubled. Using the MRF approach, it is assumed that the interaction between the rotating part (electrode) and the static part (baffles) is weak, which is feasible for most of the stirred tanks since the relationship between the impeller diameter and the diameter of the tank is low ($D/T < 0.5$) [20]. The system of this work is slightly above that ratio ($D/T = 0.52$), so the effect of simulating the steady-state at two different positions of the external bars concerning the positions of the baffles was examined. A simulation was performed with the external bars aligned to the baffles (Fig. 2A) and another with the external bars rotated 45° to the baffles (Fig.2B).

The meshes used in this analysis are tetrahedral and conformal meshes throughout the fluid domain. The meshes were made in the Ansys Meshing® preprocessor module and attention was paid to keep the geometrical quality values inside the acceptable cell range. The characteristics of the meshes in the case of 45° are shown in Table 2. To analyze the case at 0°, a mesh made up of 1 435 505 elements declared already independent in a recently published study [21] was used.

Once the steady-state flow field calculation was completed, the dynamic state was resolved to predict the mixing time. To do this, the mesh was patched with a 10 mL volume sphere at the start of the simulation in the same position as in the injection of the experiments (*see* Section 2.2). This patch helps to establish the initial condition in those cells that the tracer mass fraction equals 1 and the rest is 0. Several sampling points including the locations of the conductivity probes were declared to sample the tracer mass fraction in time. The time step used was 0.001 s with a maximum of 40 sub-iterations. The convergence criterion for each assigned time step was 10^{-5}. The agitation velocity in the tracer dynamics solution was performed at 150 rpm.

Table 1
Generation term of Eq. 6 and its associated constants. Taken from: [15].

κ-ε model	Term S_ε of Eq. (6)	Constants
Standard	$\rho\left(C_1\frac{\varepsilon}{\kappa}P_\kappa - C_2\frac{\varepsilon^2}{\kappa}\right)$	$C_1 = 1.44$, $C_2 = 1.92$, $\sigma_\kappa = 1$, $\sigma_\varepsilon = 1.3$
Realizable	$\rho\left(C_1 S_\varepsilon - \frac{C_2\varepsilon^2}{\kappa + \sqrt{\upsilon\varepsilon}}\right)$	$C_1 = max\left[0.43; \frac{\eta}{\eta+5}\right]$, $C_2 = 1.9$, $\eta = S\frac{\kappa}{\varepsilon}$, $S = \sqrt{2S_{ij}S_{ij}}$, $\sigma_\kappa = 1$, $\sigma_\varepsilon = 1.2$
RNG	$\rho\left(C_1\frac{\varepsilon}{\kappa}P_\kappa - \alpha\frac{\varepsilon^2}{\kappa} - C_2\frac{\varepsilon^2}{\kappa}\right)$	$C_1 = 1.42$, $C_2 = 1.68$, $\eta_0 = 4.8$, $\eta = S\frac{\kappa}{\varepsilon}$, $\beta = 0.012$, $C_\mu = 0.0845$, $\sigma_\kappa = 1$, $\sigma_\varepsilon = 1.3$, $\alpha = C_\mu\eta^3\frac{1 - \eta/\eta_0}{1 + \beta\eta^3}$

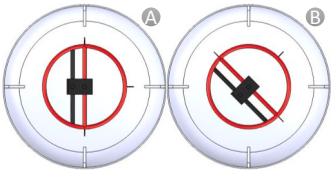

Fig. 2. Alignments at (A) 0° and (B) 45°.

Table 2
Quality parameters and the number of mesh elements.

Mesh	Cells	Max. Skewness	Min. Orthogonality
Coarse	880 895	0.85	0.20
Medium	1 707 850	0.84	0.22
Fine	3 515 686	0.84	0.18

3. Results and discussion

3.1. Performance of the κ-ε models

The comparison of the performance of the three models was carried out by solving with each of them the meshes of Table 2 at the agitation velocity of 150 rpm. To compare the results, the velocity profile was extracted in a line defined by the points *P1* ($x = 0$, $y = 0.252$ and $z = 0$) and *P2* ($x = 0.135$, $y = 0.252$ and $z = 0$). The profiles were sampled at the top of the electrode ($y = 0.52$) because in that section the fluid suction inside the rings takes place. The axial velocity profiles (V_{ax}) obtained with the three types of κ-ε models were normalized by dividing them by the typical electrode speed ($V_{tip} = \pi ND$) and plotted as a function of the normalized x position with the radius of the tank ($0.5\ T$), the results are shown in Fig. 3.

In the case of the standard model, the profiles calculated with the coarse and medium meshes agree quite well, but the fine mesh profile predicts higher negative axial velocity values inside the rings ($0.1 \leq x\ /\ 0.5\ T \leq 0.6$), and positive axial velocity values in the upper zone ($0.64 \leq x\ /\ 0.5\ T \leq 0.76$) (Fig. 3A). This behavior avoids obtaining an independent solution of the mesh with the standard model. The RNG model shows a similar negative axial velocity trend, however, the fine mesh shows a slightly different trend in the slope of change in axial velocity

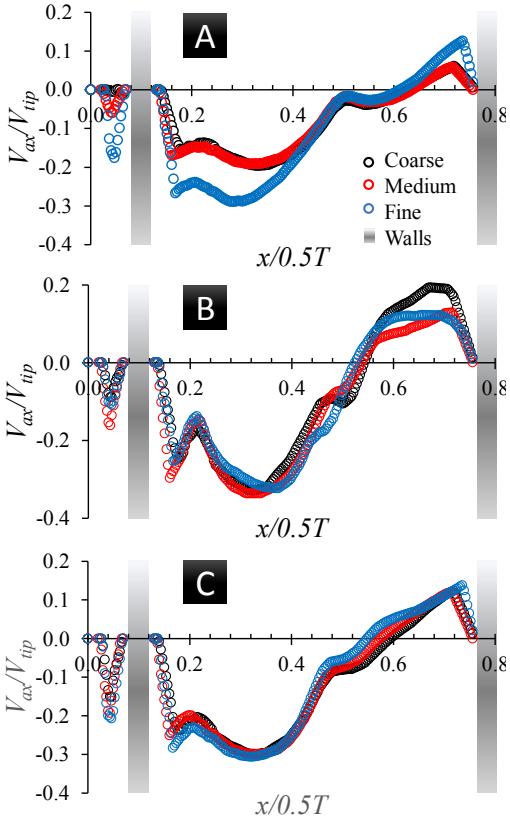

Fig. 3. Normalized profiles of axial velocity along the normalized x-axis using the κ-ε (A) standard, (B) RNG and (C) realizable models at the agitation velocity of 150 rpm.

from negative to positive ($0.4 \leq x\ /\ 0.5\ T \leq 0.6$), moreover, the magnitude and location of the positive axial velocity peak are different between the three meshes ($0.53 \leq x\ /\ 0.5\ T \leq 0.76$) (Fig. 3B). Finally, the axial velocity profiles obtained with the realizable model show a similar trend with the three meshes up to the baffle wall ($x/0.5\ T < 0.76$). Also, the "*typical behavior*" of mesh independence is observed, because as the mesh contains more elements, the solution tends to the values of the fine mesh (Fig. 3C).

The velocity profiles in Fig. 3 predicted by the different turbulence models have a similar trend. In contrast, the prediction of turbulent variables is affected by the choice of the turbulence model. The standard model predicts higher magnitude values of turbulent kinetic energy (κ) compared to the other two models because the tangential flow predominates in most of the plane and is only interrupted by the baffles (Fig. 4A). In the case of the RNG model, highest values of κ are generated by the sweep of the external bars, but the model fails to predict the recirculation of the fluid produced by the upper deflector, generating a disconnection of the stream that results in an overprediction of κ in that area (Fig. 4B). The behavior of κ predicted by the realizable model shows a distribution with the best physical sense since the greatest κ is generated by the sweep of the external bars of the electrode, as they drive the flow radially towards the tank walls. This model predicts streamlines that are not only dominated by the tangential component, but also by the radial component toward the tank walls (Fig. 4C).

The deficiencies in the prediction of the standard and RNG models can be attributed to the limitations to predict the average flow in the zones of high deformation and recirculation such as those produced in liquid by the interaction of the external bars to the rings and baffles [22]. In contrast, the realizable model allows to better capture the streams of the rotating electrode due to the improvements in the formulation of the energy dissipation rate equation based on the correction for the local deformation rate and fluid rotation (see Table 1 and Ref. [23]). Also, the realizable model allowed greater numerical stability during the solution and rapid convergence, which indicates that for this system, this model would be more effective from an engineering analysis.

3.2. Flow characterization with integral parameters

Axial flow, defined in Eq. (9), is used to evaluate the circulation induced by helical impellers [24] and multiple impeller systems [25]:

$$Q_{ax}(y) = \int_0^{0.5T}\int_0^{2\pi} |V_{ax}{}^{+}|d\theta dr = \int_0^{0.5T}\int_0^{2\pi} |V_{ax}{}^{-}|d\theta dr \tag{9}$$

where $Q_{ax}(y)$ is the flow in $m^3{\cdot}s^{-1}$ obtained by integrating the positive or negative axial velocity (V_{ax}^{+} or V_{ax}^{-}) in the transversal surface of the tank located at the height y. The radial flow is calculated using the Eq. (10).

$$Q_{rad}(r) = \int_0^{2\pi}\int_0^{H} |V_{rad}{}^{+}|dyd\theta = \int_0^{2\pi}\int_0^{H} |V_{rad}{}^{-}|dyd\theta \tag{10}$$

where $Q_{rad}(r)$ is the flow in $m^3{\cdot}s^{-1}$ obtained by integrating the positive or negative radial velocity (V_{rad}^{+} or V_{rad}^{-}) on the radial surface of the tank located at radius r. The $Q_{ax}(y)$ was calculated on ten iso-clip transverse surfaces (Fig. 5A) and $Q_{rad}(r)$ on ten iso-clip concentric surfaces (Fig. 5B).

As seen in Fig. 6A, the profile of $Q_{ax}(y)$ increases in magnitude with increasing rpm, always finding its lowest value at the bottom of the tank ($y/H = 0.1$). Two peaks a of $Q_{ax}(y)$ are located at y/H equal 0.8 and 0.3 indicating that the flow is divided axially into two main circulation zones. In Fig. 6B it is observed that the magnitude of $Q_{rad}(r)$ increases as it reaches the tank wall, reaching the highest value at $r/0.5\ T = 0.7$. This profile is because the external bars located at $r/0.5\ T = 0.52$ repel the fluid towards the tank walls, generating high velocities between the tank wall and the rings, which is consistent with the zones of high turbulence intensity in the local analysis of Martínez et al. [13]. By contrasting the results obtained from the simulations with the different angles

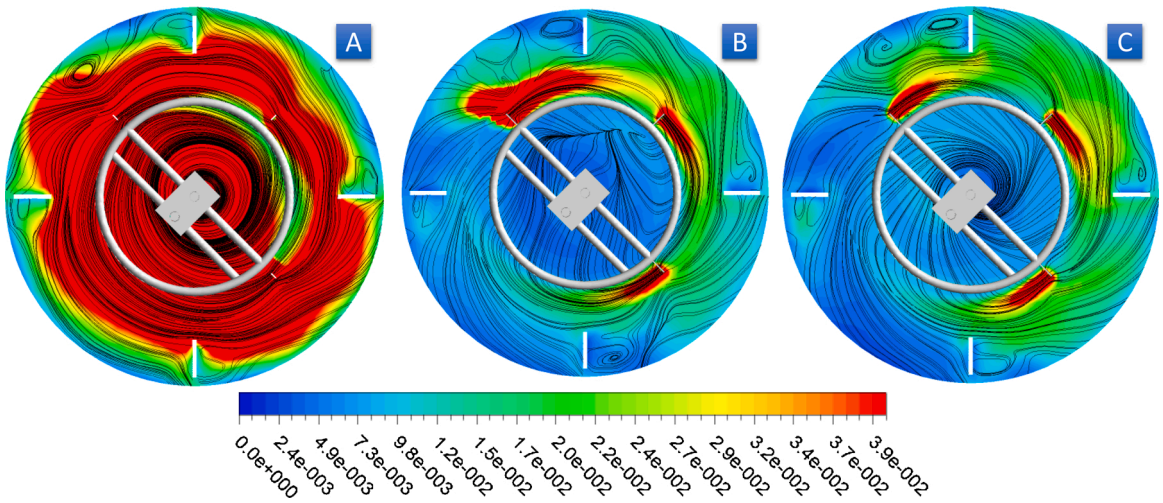

Fig. 4. Contours of κ in $m^2 \cdot s^{-2}$ and streamlines in the transverse median plane of the tank ($y/H = 0.5$) predicted by the mean mesh and the κ-ε (A) standard, (B) RNG, and (C) realizable models.

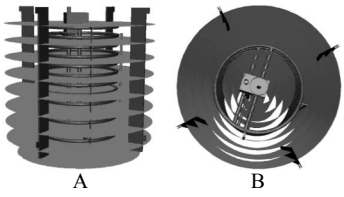

Fig. 5. Surfaces defined to calculate (A) axial flow and (B) radial flow.

concerning the baffles, it is possible to observe that for both flows higher values are obtained by placing the external bars of the baffles at 45°, especially where the flows reach their peak values. Based on the values of Fig. 6 it is possible to calculate the axial average flow ($Q_{V_{ax}}$) and the radial average flow ($Q_{V_{rad}}$) using Eqs. (11) and (12), respectively.

$$Q_{V_{ax}} = \frac{\int_0^H Q_{ax}(y)dy}{\int_0^H dy} \tag{11}$$

$$Q_{V_{rad}} = \frac{\int_0^{0.5T} Q_{rad}(r)dr}{\int_0^{0.5T} dr} \tag{12}$$

To normalize $Q_{V_{ax}}$ and $Q_{V_{rad}}$ the values are divided between ND^3, when doing this operation the axial ($N_{Q_{V_{ax}}}$) and radial ($N_{Q_{V_{rad}}}$) numbers are obtained, respectively, and are shown in Table 3. The mean value of $N_{Q_{V_{rad}}}$ decreases at 230 rpm but increases again at 500 rpm, meanwhile, the mean value of $N_{Q_{V_{ax}}}$ decreases at 230 rpm. The tendency of both numbers indicates that at high speeds (>230 rpm) the circulation cannot be improved.

Nevertheless, as observed in Fig. 6, the values of both flows are higher with the simulations at the 45° position, having an average difference between simulations by 8.6% for the axial flow and by 7.0% for

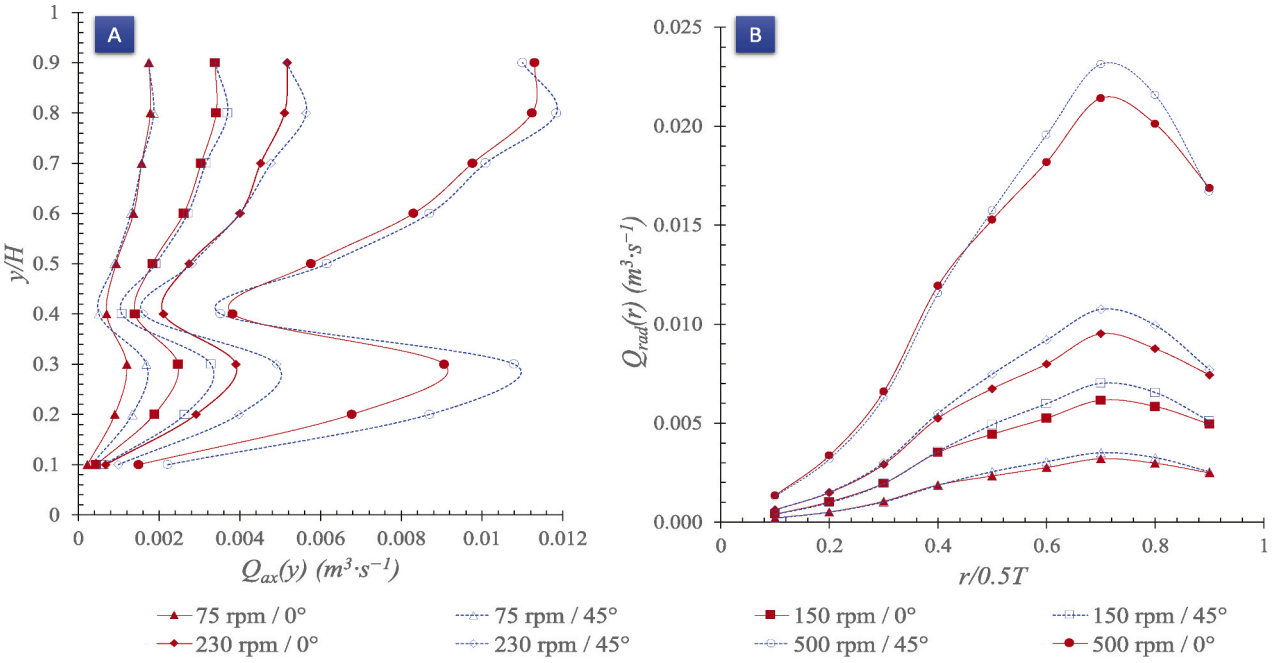

Fig. 6. Flow profiles (A) axial and (B) radial at different agitation velocities obtained with the two different alignments in the MRF simulations.

Table 3
Numbers of axial and radial flow obtained at different stirring speeds and with the simulations at different alignment positions of the external bars concerning the baffles.

N (rpm)	0° $N_{Q_{V_{rad}}}$	45° $N_{Q_{V_{rad}}}$	Mean $N_{Q_{V_{rad}}}$	0° $N_{Q_{V_{ax}}}$	45° $N_{Q_{V_{ax}}}$	Mean $N_{Q_{V_{ax}}}$
	–	–	–	–	–	–
75	0.56	0.60	0.58	0.34	0.36	0.35
150	0.54	0.59	0.57	0.33	0.36	0.35
230	0.54	0.59	0.56	0.33	0.36	0.34
500	0.56	0.58	0.57	0.33	0.35	0.34

the radial flow. Dividing the volume of the tank between the average flows $Q_{V_{ax}}$, and $Q_{V_{rad}}$, it was obtained the axial and radial circulation times ($t_{c\text{-}ax}$ and $t_{c\text{-}rad}$), respectively. Fig. 7 shows the axial and radial circulation times calculated with the values of $Q_{V_{ax}}$ and $Q_{V_{rad}}$ generated by the simulations at 0° and 45°. Both circulation times show a logarithmic decay trend as the agitation velocity increases, achieving lower radial circulation times than axial circulation. This behavior in circulation times indicates that fluid particles travel faster through the radial section of the tank than through the axial section, maintaining a difference of approximately 40% at all agitation velocities. To compare the axial circulation times obtained with this electrode, the product $t_{c\text{-}ax} \cdot N$ is calculated, obtaining an average value of 16.8. This value is in the range of that reported for helical impellers ($14 < t_{c\text{-}ax} \cdot N < 18$) [26], showing that this electrode configuration has similar capacities as the mixer devices conventionally used.

When using RANS models, the power number (N_P) is usually calculated as shown in Eq. (13).

$$N_P = \frac{2\pi NM}{\rho N^3 D^5} \tag{13}$$

where M is the torque in N·m obtained by integrating the pressure and viscous forces on the surface of the moving walls using the angular momentum balance [27]. Another important additional number to characterize the stirred tanks is the pumping number, which is defined in Eq. 14.

$$N_Q = \frac{Q}{ND^3} \tag{14}$$

where Q is the flow in $m^3\ s^{-1}$ that is obtained by integrating the positive radial velocity over a radial surface that surrounds the electrode. The ratio between N_Q and N_P defines the pumping capacity (η_{pump}), a parameter that indicates how much of the energy that is supplied to the system is used to move the fluid.

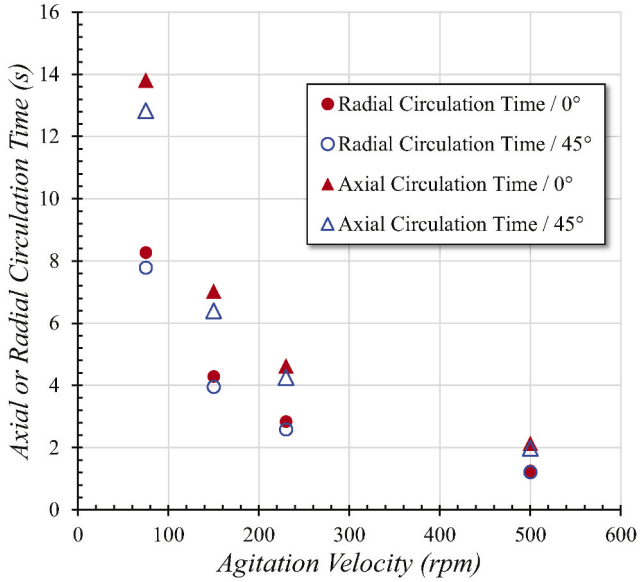

Fig. 7. Axial and radial circulation times as a function of agitation velocity.

As seen in, the N_P values change depending on the alignment position, since at 75 rpm the value is 10% greater at 45°, while at 500 rpm the value at 45° continues to be greater by 4.8%. A similar trend occurs with the N_Q values, although the differences are slightly higher (12% at 75 rpm and 5% at 500 rpm). The dependence of these values on the alignment position must be taken into account in complex geometries when using the MRF approach, as this may affect decisions in the design improvement process using CFD tools. The average N_P indicates that from 230 rpm it remains constant, something that does not happen with the average N_Q, since it fluctuates slightly. As can be seen, the values of η_{pump} remain constant as it increases, which suggests that pumping capacities cannot be improved with an increasing RRE velocity. Nevertheless, the calculus of N_Q only considers the radial flow discharged by the electrode which is a disadvantage for the actual complex flow since as observed in Fig. 6A, this is axially divided into two circulation zones. This fact prevents the ratio between N_Q and N_P (η_{pump}) adequately describes the efficiency of this system. On the other hand, the $N_{Q_{V_{ax}}}$ considers the transport of the fluid through these different circulation zones. Calculating the radius between the mean values of $N_{Q_{V_{ax}}}$ (Table 3) and N_P (Table 4), it was obtained 0.0773, 0.0780, 0.0777, and 0.0772 for the velocities of 75, 150, 230, and 500 rpm, respectively, which indicate that the best efficiency of the agitation velocities tested in this work is achieved at 150 rpm. The present results agree with previous experimental observations in the application of this electrochemical reactor in the reduction of hexavalent chromium [28]. As shown, the average parameters in Table 4 are similar order of magnitude as the radial impellers, e.g., the Rushton turbine in a turbulent regime, which reports power and pumping numbers ranges of $4.13 < N_P < 6.07$ and $0.65 < N_Q < 0.75$, respectively [29], resulting in a range of $0.12 < \eta_{pump} < 0.16$ for pumping capacity. This is particularly important since it could mean that the flow characteristics of the Rushton Turbine such as the high shear and the vortices generated at the tips of the blades could appear in the RRE.

3.3. Mean flow pattern analysis

To qualitatively analyze the pattern developed by the dynamic electrode, the streamlines generated at 150 rpm colored by the axial velocity for the baffles and external bars aligned at 0° and 45° are shown in Fig. 8A and Fig. 8B, respectively. As can be appreciated, the external bars of the RRE mainly produce the movement of the fluid propelling it towards the lateral tank wall. An interesting issue is the presence of the pink-colored positive axial stream coming from the circulation loops at the bottom of the tank to the circulation loops in the upper part, as is shown in Fig. 8A. This interaction between the upper and lower circulation loops is not predicted with such intensity by the case of 45° alignment (Fig. 8B); because in this case the flow is dominated by the discharge stream of the exterior bars. Fig. 9 shows the detail of the axial profiles sampled in lines D (outside of the electrode) and E (inside of the electrode) to show the behavior of the flow around of cathodes and

Table 4
Numbers of power and pumping obtained at different agitation speeds and with the simulations at different alignment positions of the external bars concerning the baffles.

N (rpm)	45°		0°		Mean		
	N_P	N_Q	N_P	N_Q	N_P	N_Q	η_{pump}
75	4.79	0.84	4.28	0.74	4.53	0.79	0.17
150	4.63	0.81	4.29	0.72	4.46	0.77	0.17
230	4.57	0.81	4.26	0.71	4.42	0.76	0.17
500	4.53	0.79	4.31	0.75	4.42	0.77	0.17

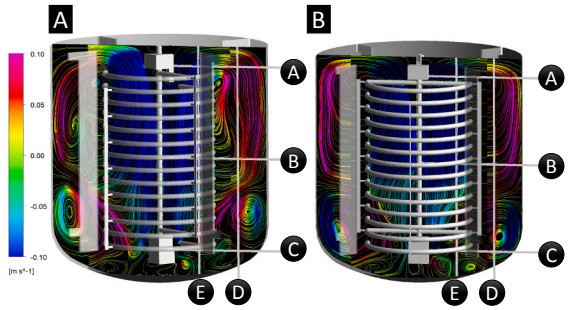

Fig. 8. Streamlines colored by axial velocity developed at 150 rpm. (A) MRF simulation at 0° and (B) MRF simulation at 45°.

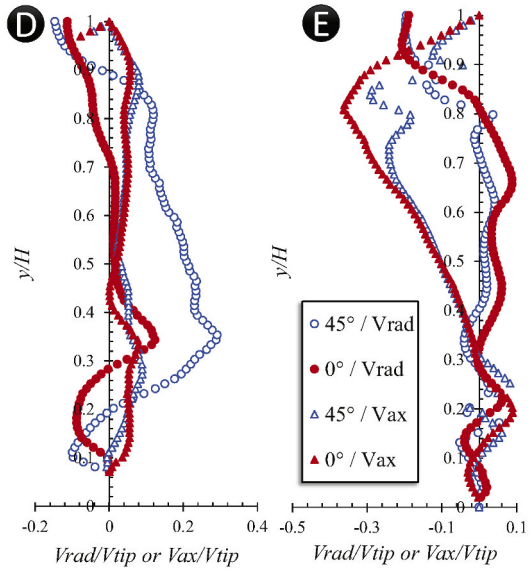

Fig. 9. Axial profiles sampled on the lines D and E marked in Fig. 8 of axial and radial velocities.

anodes surface. As seen, in the profile of the radial velocity of Fig. 9D, the radial velocity reaches its maximum value at the height of $y/H = 0.35$, and it is right where the flow is divided into two main lateral recirculation loops (Fig. 8 B). The radial velocity values of Fig. 9D at 45° of alignment was higher respect to the alignment of 0°, due to the presence of the external bars in the sampled plane (Fig. 8). The axial velocity in the profile of Fig. 9D shows two peaks that change their position as a function of alignment. At 45° of alignment, the peaks are located at $y/H = 0.27$ and $y/H = 0.86$ and both has a magnitude of *0.08 Vtip*, whereas, at 0° of alignment, the peaks are located slightly above, the first peak at $y/H = 0.33$ and the second peak at $y/H = 0.88$ with a magnitude of *0.05 Vtip* and *0.07 Vtip*, respectively. These peaks represented the limits of the main two lateral recirculation loops of Fig. 8, which were different for both alignments.

Fig. 10 shows the detail of the radial profiles sampled in the lines A, B, C. The direction of the two main lateral recirculation loops can be concluded with the radial profiles of Fig. 10. The axial velocity of Fig. 10B shows a positive sign outside the rings ($x/0.5\ T > 0.52$) indicating that the fluid is transported to the top of the tank, whereas inside the rings ($x/0.5\ T < 0.52$) shows a negative axial velocity. The results obtained from the simulations in both alignments follow the same axial velocity trend. The radial velocity of the Fig. 10B at the 0° alignment shows low positive velocities with a peak at $x/0.5\ T = 0.5$, while the 45° alignment shows a sharp change at $x/0.5\ T = 0.58$ due to the sweep of the external bar. The axial velocity trend of Fig. 10A has the same tendency of the profiles of Fig. 10B, but the negative velocities inside the rotating electrode were largest as they coincided with the suction region. The radial velocity of the Fig. 10A, shows a negative sign, that indicates the suction of the fluid into the rings. The radial velocity of Fig. 10A in both alignments shows a similar trend. The axial velocity of Fig. 9E confirms that the upper recirculation loop transports the fluid towards the lower zone of the tank within the rings until $y/H = 0.3$.

The lower lateral recirculation loops rotate in the opposite direction of the upper ones (blue streamlines at the lower part of the tank wall of Fig. 8). Inside the rings, the discharge flow from the upper recirculation loop dominates until $y/H = 0.3$, where axial and radial velocities are around zero (Fig. 9E). This fact indicates that the streams from the discharge of the upper recirculation loop and the streams from the bottom recirculation loop collide, producing recirculation spots of low axial velocity (see the yellow-colored small loops at the bottom of the tank in Fig. 8). These recirculation spots are known as stagnation zones. By comparing the profiles of the axial velocity shown in Fig. 10A and B respect to the profiles of Fig. 10C, it can be seen that the trend changes dramatically, since there are negative and positive values in the area outside ($x/0.5\ T > 0.52$) and inside ($x/0.5\ T < 0.52$) the rings. The peaks of the values of the axial and radial velocity profiles of Fig. 10C, strongly change their position depending on the alignment of the static walls concerning the moving walls, with which it can be inferred that the macrostructures that are located there, are highly complex and three dimensional. This effect is also observed at the bottom of the tank ($0 < y/H < 0.3$) in the axial profiles of Fig. 9.

The generation of the stagnation zones may explain why, despite the increase in stirring speed, the Q_{ax} does not increase significantly at the height of $y/H = 0.1$ (Fig. 6A). Moreover, the existence of these stagnation zones may explain the reactor behavior, when its performance using this kind of electrode was experimentally evaluated to achieve the electrochemical reduction of hexavalent chromium. It was found that increasing the agitation velocity beyond 150 rpm considerable reductions in treatment time, were no reached [28]. Previously, to improve the pumping capacity of this electrode, it was decided to incorporate different elements into the geometry, such as internal bars [14] or pitched blade impellers [30] inside the rings. These actions increased the axial flow but were unable to eliminate the stagnation zones at the bottom of the tank since the stream coming from the loop produced by the radial flow was not considered.

3.4. Identification of areas of high turbulence

In processes such as electrocoagulation or electroflotation, the electro-dilution of a metal ion from the sacrificial anode is carried out to promote flocculation of the pollutants. The generation of these agglomerated particles (flocs) is mainly dependent on to two factors: (1) the adequate dispersion of metal ions throughout the volume to interact with the contaminants present and (2) the formation of particles with the largest possible diameter to easily remove them from the treated effluent [31]. These factors make the process dependent on a balance between good mixing and the shear stresses produced by stirring the solution. The movement of the stirrer does not have to be so high to cause the agglomerates to break, nor so low to produce a poor mix of the species inside the reactor. A variable that allows estimating the force with which the fluid is deformed is the strain rate (S_R) defined in Eq. (15).

$$SR = \left[2\frac{\partial U_i}{\partial x_j}S_{ij}\right]^{1/2} \tag{15}$$

Where the strain tensor (S_{ij}), defined as in Eq. (16):

$$S_{ij} = \frac{1}{2}\left(\frac{\partial U_i}{\partial x_j} + \frac{\partial U_j}{\partial x_i}\right) \tag{16}$$

A parameter that indicates the magnitude of fluid rotation is vorticity

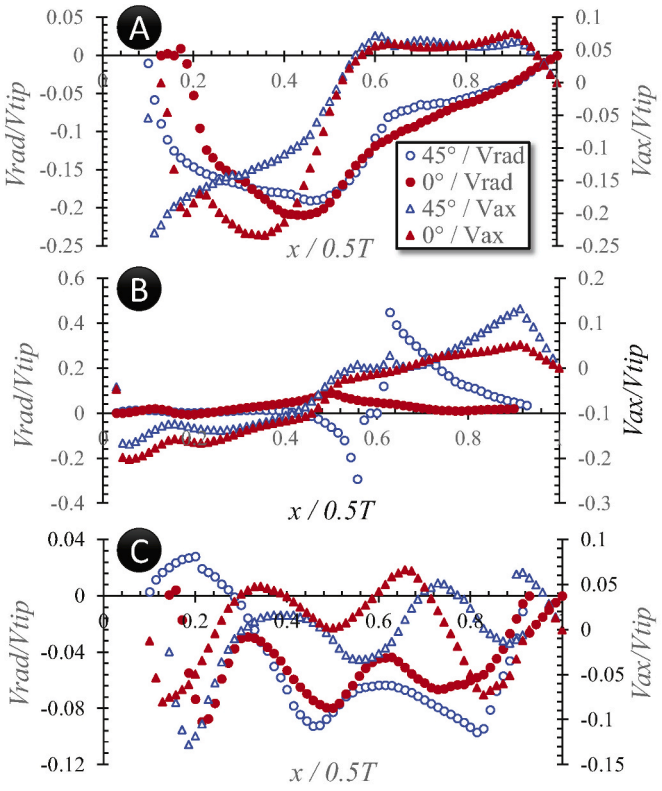

Fig. 10. Radial profiles sampled on the lines A, B, and C marked in Fig. 8 of axial and radial velocities.

(ω), defined by the rotational velocity field as shown in Eq. (17).

$$\omega = \nabla \times u \tag{17}$$

Fig. 11 shows iso-surfaces of the S_R and ω caused in the fluid by the movement of the rotating ring electrode. The iso-surfaces were generated with the simulations at the 45° position with respect to the baffles

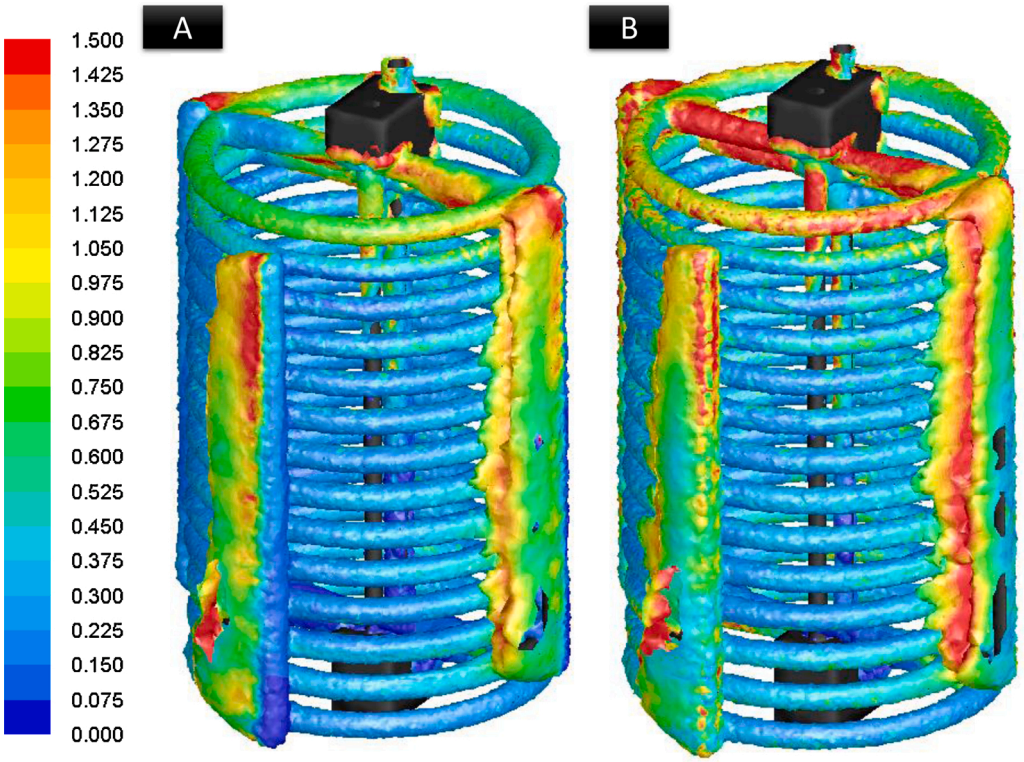

Fig. 11. Iso-surfaces of (A) the strain rate and (B) vorticity generated in the fluid at the agitation velocity of 150 rpm colored by the turbulent dissipation energy, ε (scale in $m^2 \cdot s^{-3}$). The threshold value of the strain rate and vorticity is 75 s^{-1}.

since it is desired to observe the influence of the external bars over the flow. The iso-surfaces generate three-dimensional structures that represent the threshold value, which allows spatial observation of the areas where the variable is present at that magnitude. In the numerical evaluation with RANS models of similar technologies such as flocculators, ε has been used to estimate the "*velocity gradient*" (G), defined as $G = (\varepsilon/\nu)^{1/2}$, where ν is the kinematic viscosity of the fluid in $m^2 \cdot s^{-1}$ [32]. The G is a parameter that serves to characterize breakage that will cause agitation to the flocs. Owing to this fact, the iso-surface is colored by ε to identify the structures that dissipate the greatest amount of energy and therefore cause the most floccules to break.

The structures generated by the S_R (Fig. 11 A) and ω (Fig. 11 B) are very similar. However, it is possible to notice that there are regions that more intensely in the case of ω are colored. One of them is due to the upper circulation loops (Fig. 8), in that area the structure is colored in red, indicating that the rotation of the fluid dissipates a large amount of energy (Fig. 11 B). One fact that they coincide on both iso-surfaces is that the structures generated by the external bars to the rings usually generate areas of high dissipation of turbulent kinetic energy (Fig. 11), so that is where the flocs will be exposed to higher velocity gradients, making them susceptible to break. Another important aspect is that the iso-surface covers the surface of the rings, which could indicate that locally the reduction of the diffusion boundary layer is promoted, improving the mass transfer of the metallic species from the electrode to the bulk liquid, during the process such as electrocoagulation.

To analyze the effect of the agitation velocity on these variables, an average volumetric integral in the volume of the fluid was performed using Eq. (18).

$$\frac{1}{V}\iiint \phi dV = \sum_{i=1}^{n} \phi_i |V_i| \tag{18}$$

Where ϕ represents any flow variable (i.e. ω or S_R) and V_i the volume of the cell. Fig. 12 shows the average value obtained in the simulations at the positions of 45° and 0° in each part of the computational domain and in the whole volume. Comparing the trend of the strain rate (Fig. 12A) and the vorticity (Fig. 12B), as a function of the agitation speed, it is observed that they have very similar behavior, since in magnitude they grow in the same way as the stirring speed increases. It is also shown that the area where these variables are most concentrated in the RRF, since it is the volume that is most exposed to the electrode sweep.

By using a realizable κ-ε model, it is possible to calculate the turbulence intensity (I). When estimating I, it is possible to correlate the benefits of macro mixing in electrochemical processes, such is the case of the electrocatalytic phenol hydrogenation process since it was observed that the hydraulic configuration of the cell that promoted higher I achieved better experimental yields [33]. Turbulence intensity is the ratio of velocity fluctuations caused by turbulent chaotic motion to average flow velocity. These velocity fluctuations are calculated from the turbulent kinetic energy (κ) as shown in Eq. (19).

$$I = \frac{u'_i}{U_i} = \frac{\sqrt{2/3\,k}}{U_i} \tag{19}$$

As a general rule, the intensity of turbulence less than 10% is considered as a low intensity of turbulence, when it exceeds 15%, the intensity of turbulence is considered high [34]. From the histogram in Fig. 13 it can be seen that the distribution peak shifts to the right as the agitation velocity increases. At 75 rpm, 100% of the cells are below 10% of I. At 150 rpm, only 6% of the cells exceed 15% of I, and increasing the speed to 230 rpm, 19% of cells more exceed 15% of I. When the reactor is operated at 500 rpm, 3% of the cells remain below 15% of I. The difference between the distribution of I between the agitation velocity of 150 rpm and 230 rpm could explain what was experimentally observed by Mollinedo et al. [28] since there is only a difference of 2 min between the electrolysis times to achieve 100% reduction of hexavalent chromium from rinsing waters of the electroplating industry.

Fig. 14 shows the distribution of I in the axial plane located between baffles generated with the results of both simulations alignment to depict the changes in the local results. In both alignments, the highest values of I are located in the upper part of the RRE at the different agitation velocities. On the other hand, the bottom of the tank remains with a low I despite the increase of rpm that produces a flow disconnection at the bottom of the inside of the rings. The zones of high I showed in the contours at 0° of alignment (Fig. 14A – D) are less than the zones shown in the simulations at 45° (Fig. 14E–H). The distribution of I can be attributed to the fact that the frozen flow field obtained with the 45° alignment is dominated by the radial flow generated by the external bars. They create high turbulence in the periphery of the electrode. On the other hand, the frozen flow field at 0°, the flow generated by the external bars is dampened by the baffles causing a decrease in the high turbulence areas located next to the external bars.

To show the structures of the trailing vortices generated by the rotating electrode, the *Q-criterion* was calculated, which has been applied in different incompressible flow systems to visualize the fluid regions connected by the second invariant term of the velocity gradient. Although RANS models are known to model the entire energy turbulent spectrum, it has been reported that with them it is possible to predict and visualize the main structures of the vortices that are generated in the fluid in stirred tank systems [35]. *Q-criterion* is defined in Eq. (20), where it can be seen that those regions where the magnitude of vorticity prevails over the magnitude of the deformation rate will be the regions considered [36].

$$Q = \frac{1}{2}\left(\|\omega\|^2 - \|S\|^2\right) > 0 \tag{20}$$

Fig. 15 shows the iso-surface obtained at the agitation velocity of the electrode at 500 rpm. It is interesting to note that in contrast to Fig. 11, the vortex structures do not detach from the entire height of the external bars, but only from the tips of the bars, which in the future could be

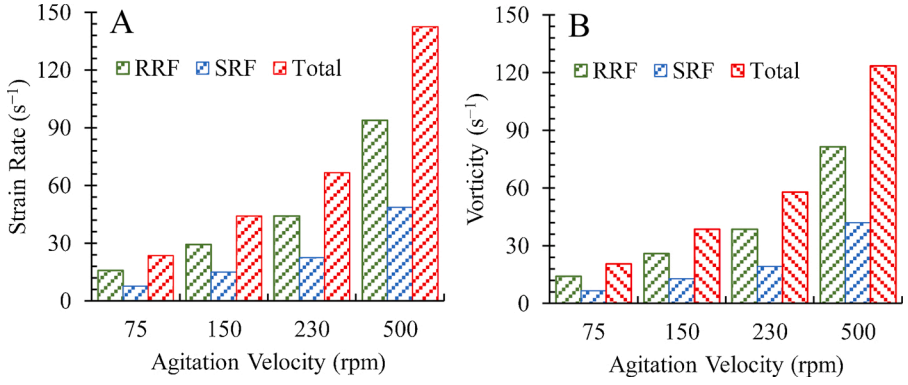

Fig. 12. The average volumetric integral of the (A) deformation rate and (B) vorticity at different agitation velocities.

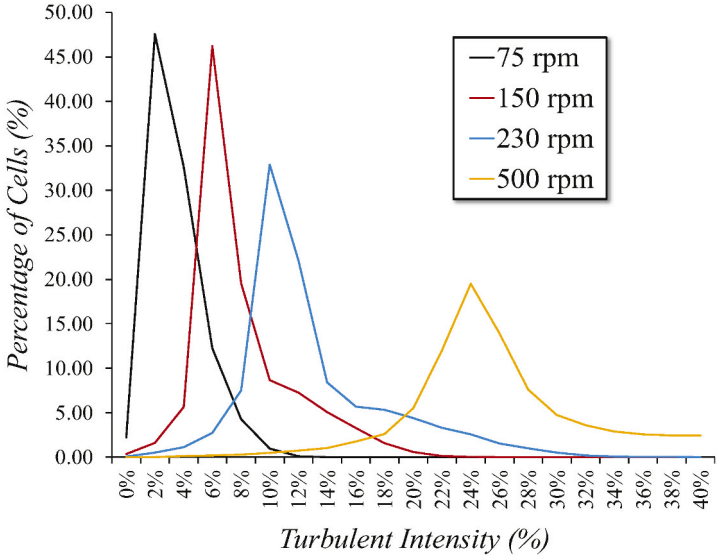

Fig. 13. Distribution of the turbulent intensity in the computational domain at the different agitation velocities obtained with the simulations at 45°.

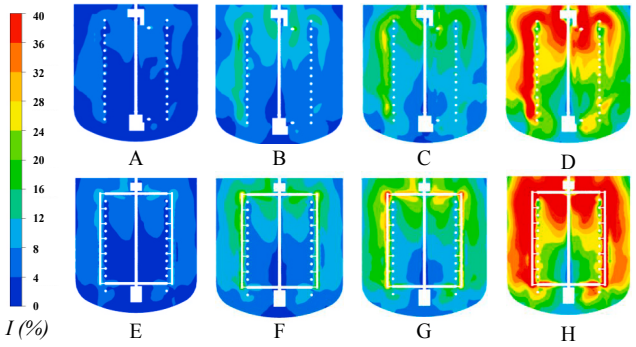

Fig. 14. Contours of *I* in the axial plane located between baffles. Alignment at 0° (A) 75 rpm, (B) 150 rpm, (C) 230 rpm and (D) 500 rpm. Alignment at 45° (E) 75 rpm, (F) 150 rpm, (G) 230 rpm, and (H) 500 rpm.

redesigned to reduce the dissipation of energy in those areas. Besides, it can be seen that the agitation also generates vortices in the upper internal bars with zones of high turbulence intensity, this indicates that these bars act as an impeller, as they pump the fluid into the rings achieving the high axial flows seen in Fig. 6 A, at the height of $y/H = 0.8$. From the design point of view, these regions of the electrode geometry can be improved to dissipate less energy and thereby achieve an increase in the efficiency of the electrode when applied to some electrochemical process for wastewater treatment. The MRF simulations at the alignment of 0° show more developed vortex structures than the simulations at 45°. The difference must be due to the frozen flow field obtained with the alignment at 0° is less influenced by the discharge flow from the exterior bars, allowing describe better the interaction between circulation structures as shown in Fig. 8.

3.5. Mixing time

This section presents the simulation and experimental results to evaluate the mixing of an inert tracer at 150 rpm. Fig. 16 shows the average experimental points of the 15 tests, marking the standard deviation at each point by the error bars. As seen in Fig. 16 in one second, the simulation at 45° slightly overestimates the range of the experimental measurements, while at 0° the curve falls within the experimental range. Between 3 and 8 s, both simulations slightly

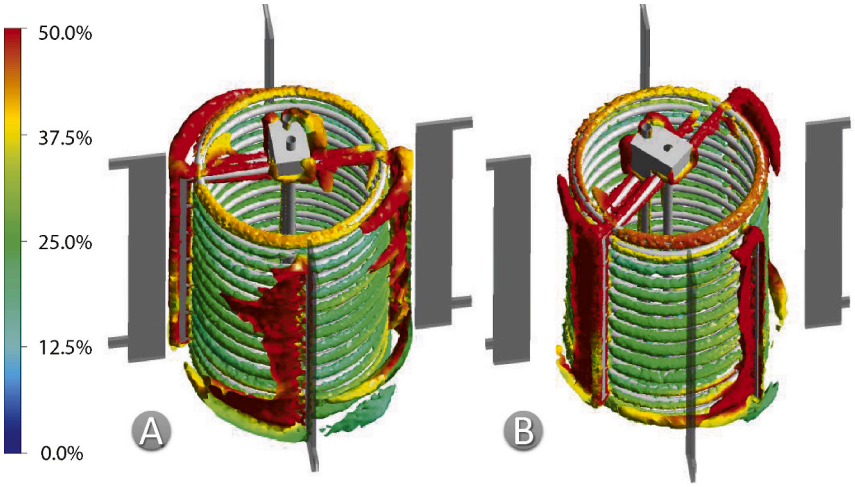

Fig. 15. Iso-surfaces of *Q-criterion* obtained with the MRF simulation at (A) 0° and (B) 45° of the baffles at an agitation velocity of 500 rpm colored by the turbulence intensity, *I* (%). The threshold value is 4816 s^{-1}.

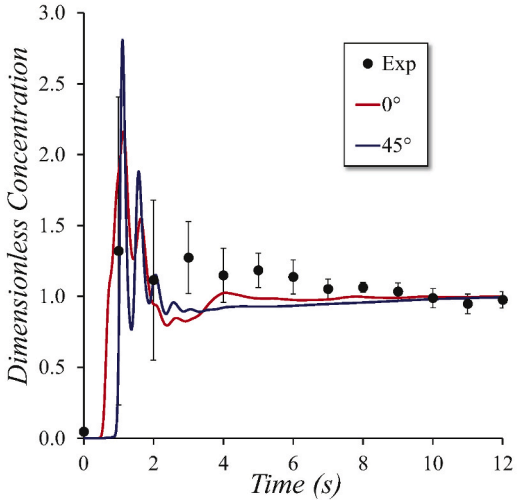

Fig. 16. Tracer dynamics described by experiments and simulations.

underestimate the experimental values, being at this time when the tracer tends to the homogeneous concentration. It is possible to observe that the underprediction is slightly higher in the 45° simulation than in the 0° simulation, which affects the θ95% calculated for each simulation, since as shown in Table 4, the simulation at 45° predicts the largest experimental deviation than the simulation at 0°. However, the experimental error of both simulations (Table 4) is below the experimental errors reported for agitated tank systems, since a maximum error of 20% has been reported [37].

The error between the prediction of the mixing time and the experiments is mainly attributed in the literature to the inability to adequately predict μ_t by isotropic models such as realizable κ-ε model since transient macro instabilities are generated in the tank between the circulation loops that are not captured by the RANS models [38]. Nevertheless, the prediction of the average flow by such models is good and allows the global properties of hydraulics to be analyzed with a good level of reliability while maintaining the engineering advantage of saving on computational resources.

To explore the detail of the tracer distribution at different times, the contour plots of the mass fraction of the tracer in the axial plane are shown in Fig. 17. In the case of 0° of alignment, at 0.5 s (Fig. 17A), the tracer is quickly transported to the center of the tank. This can be due to the upper loop is more influenced by the negative axial velocity (Fig. 8 A). On the other hand, in the alignment of 45°, at 0.5 s, the tracer travels slowly to the center of the tank (Fig. 17D) by the influence of the radial component (Fig. 8B). After 2 s, the tracer is more homogeneously distributed in the case of 0° of alignment (Fig. 17B), due to the flow field are less influenced by the discharge stream of the exterior bars and predicted a connection stream between upper and lower circulation loops increasing the convective transport of the tracer. At the same time, in the case of 45° of alignment, the tracer is concentrated in the upper circulation loops (Fig. 17E), since the frozen flow field is dominated by the discharge stream of the exterior bars, and generate circulation loops with little connection. This behavior continues up to 4 s, where the 0° alignment case shows a tracer distribution in the entire axial plane (Fig. 17C), and in the case of alignment of 45°, there is a low concentration of the tracer in the bottom of the tank (green zones, Fig. 17F). The difference of the frozen flow field obtained in both alignments causes that the θ95% calculated with the data from the alignment simulation of 45° was longer than at 0° (Table 4). The results show that θ95% at 0° is in good agreement (error 6%) with the experimental results rather than the alignment at 45°.

4. Conclusions

From the numerical analysis of flow field induced by the RRE several conclusions can be pointed out:

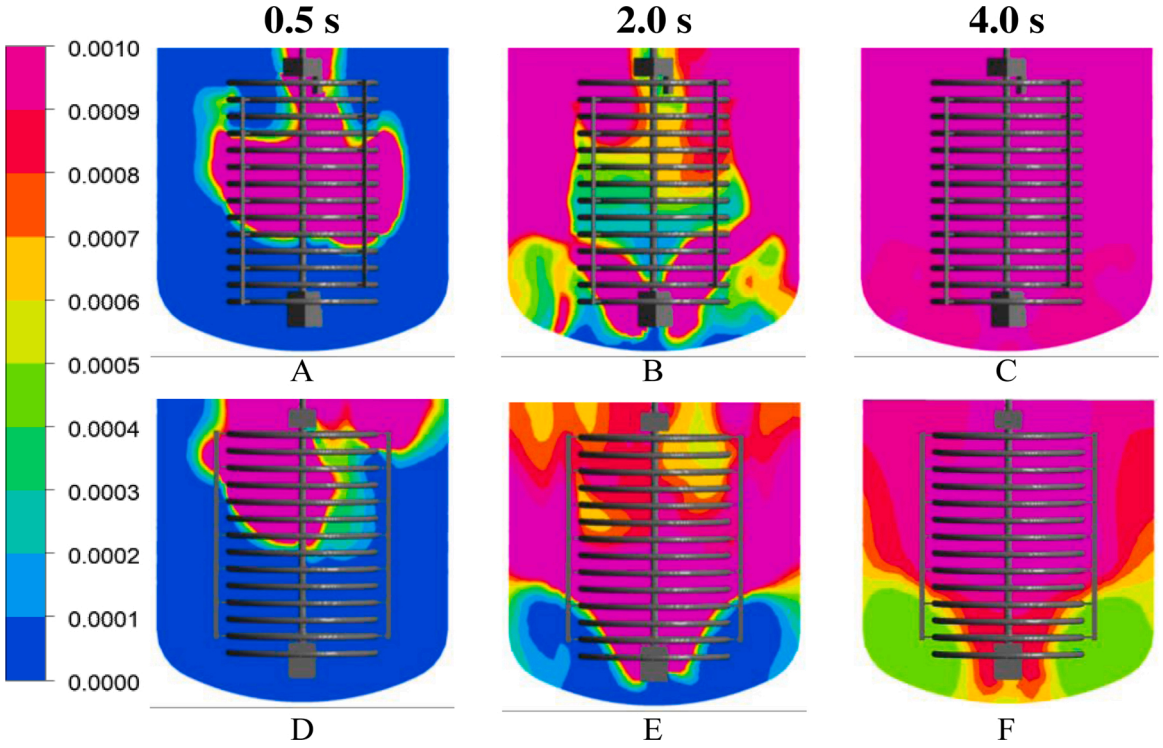

Fig. 17. Contours of the mass fraction of the tracer in the axial plane between baffles at different times. Simulation at 0° (A, B, and C), and simulation at 45° (D, E, and F).

- Comparison between κ-ε models: The realizable model shows a better capacity and stability to predict the complex flow induced by the RRE due to the improvements in its formulation. With this model, the grid independency analysis from the analysis of the flow profiles is achieved.
- Mean flow: The flow pattern is predominantly radial, caused by the external bars, as they pump the fluid towards the walls of the tank causing the formation of four main circulation loops. The internal bars promote axial flow in the center of the tank, causing the currents from the two lower loops to collide with those discharged to the center, creating stagnation zones in the lower part of the reactor.
- Position effect in the MRF simulations: in case the of the position at 45°, the external bars and baffles generate a frozen flow field dominated by the radial flow induced by the exterior bars, whereas, in the alignment 0° these radial steams are damping by the presence of baffles.
- Areas with high turbulence: The exterior bars generate the areas of high turbulence, which in future works could be changed its geometry to improve the hydraulic performance of the electrode hence the performance in the electrochemical process.
- Comparison of experiments and simulations of mixing time: The simulation at 45° over predicts 18% the experimental value of θ95%, while simulation at 0° is in good agreement (error 6%) with the experimental results.

Authorship statement

All persons who meet authorship criteria are listed as authors, and all authors certify that they have participated sufficiently in the work to take public responsibility for the content, including participation in the concept, design, analysis, writing, or revision of the manuscript. Furthermore, each author certifies that this material or similar material has not been and will not be submitted to or published in any other publication.

Authorship contributions

The specific contributions made by each author are the following:

Conception and design of study: Yáñez-Varela and Martinez-Degadillo.

Acquisition of data: Yáñez-Varela, Israel González-Neria, Rivadeneyra-Romero.

Analysis and/or interpretation of data: Yáñez-Varela, Israel González-Neria, Martinez-Degadillo, Alonzo-Garcia, Rivadeneyra-Romero.

Drafting the manuscript: Yáñez-Varela, Martinez-Degadillo, Alonzo-Garcia.

All authors discussed the results and commented on the manuscript

Declaration of Competing Interest

The authors report no declarations of interest.

References

[1] L.J.J. Janssen, L. Koene, The role of electrochemistry and electrochemical technology in environmental protection, Chem. Eng. J. 85 (2002) 137–146, https://doi.org/10.1016/S1385-8947(01)00218-2.

[2] K. Jüttner, U. Galla, H. Schmieder, Electrochemical approaches to environmental problems in the process industry, Electrochim. Acta 45 (2000) 2575–2594, https://doi.org/10.1016/S0013-4686(00)00339-X.

[3] K. Scott, Process intensification: an electrochemical perspective, Renewable Sustainable Energy Rev. 81 (2018) 1406–1426, https://doi.org/10.1016/j.rser.2017.05.189.

[4] A.S. Naje, S. Chelliapan, Z. Zakaria, M.A. Ajeel, P.A. Alaba, A review of electrocoagulation technology for the treatment of textile wastewater, Int. Rev. Chem. Eng. 33 (2017) 263–292, https://doi.org/10.1515/revce-2016-0019.

[5] L.F. Catañeda, F.F. Rivera, T. Pérez, J.L. Nava, Mathematical modeling and simulation of the reaction environment in electrochemical reactors, Curr. Opin. Electrochem. 16 (2019) 75–82, https://doi.org/10.1016/j.coelec.2019.04.025.

[6] M.A. Sandoval, R. Fuentes, F.C. Walsh, J.L. Nava, C.P. de León, Computational fluid dynamics simulations of single-phase flow in a filter-press flow reactor having a stack of three cells, Electrochim. Acta 216 (2016) 490–498, https://doi.org/10.1016/j.electacta.2016.09.045.

[7] A. Rodríguez, F.F. Rivera, G. Orozco, G. Carreño, F. Castañeda, Analysis of inlet and gap effect in hydrodynamics and mass transport performance of a multipurpose electrochemical reactor: CFD simulation and experimental validation, Electrochim. Acta 282 (2018) 520–532, https://doi.org/10.1016/j.electacta.2018.06.071.

[8] A. Choudhary, S. Mathur, Performance evaluation of 3D rotating anode in electro coagulation reactor: part II: effect of rotation, J. Water Process Eng. 19 (2017) 352–362, https://doi.org/10.1016/j.jwpe.2017.08.019.

[9] A. Choudhary, S. Mathur, Performance evaluation of 3D rotating anode in electro coagulation reactor: part I: effect of impeller, J. Water Process Eng. 19 (2017) 322–330, https://doi.org/10.1016/j.jwpe.2017.08.020.

[10] M.G. Rodríguez, R. Aguilar, G. Soto, S.A. Martínez, Modeling an electrochemical process to remove Cr(VI) from rinse-water in a stirred reactor, J. Chem. Technol. Biotechnol. 78 (2003) 371–376, https://doi.org/10.1002/jctb.746.

[11] M.G. Rodríguez R, V. Mendoza, H. Puebla, S.A. Martínez D, Removal of Cr(VI) from wastewaters at semi-industrial electrochemical reactors with rotating ring electrodes, J. Hazard. Mater. 163 (2009) 1221–1229, https://doi.org/10.1016/j.jhazmat.2008.07.114.

[12] S. Martinez-Delgadillo, H. Mollinedo-Ponce, V. Mendoza-Escamilla, C. Gutiérrez-Torres, J. Jiménez-Bernal, C. Barrera-Díaz, Performance evaluation of an electrochemical reactor used to reduce Cr(VI) from aqueous media applying CFD simulations, J. Clean. Prod. 34 (2012) 120–124, https://doi.org/10.1016/j.jclepro.2011.10.036.

[13] S. Martínez, J. Ramírez, H. Mollinedo, V. Mendoza, C. Gutiérrez, J. Jiménez, Determination of the spatial distribution of the turbulent intensity and velocity field in an electrochemical reactor by CFD, Int. J. Electrochem. Sci. 8 (2013) 274–289.

[14] O. Huerta, Y. Rodriguez, V. Mendoza, H. Mollinedo, M. Morales, S. Martínez, The effect of internal impellers on mixing in an electrochemical reactor with rotating rings electrodes, Chem. Eng. Process. Process Intensif. 88 (2015) 37–46, https://doi.org/10.1016/j.cep.2014.12.003.

[15] Z. Jaworski, B. Zakrzewska, Modelling of the turbulent wall jet generated by a pitched blade turbine impeller: the effect of turbulence model, Chem. Eng. Res. Des. 80 (2002) 846–854, https://doi.org/10.1205/026387602321143381.

[16] B.E. Launder, D.B. Spalding, The numerical computation of turbulent flows, Comput. Methods Appl. Mech. Eng. 3 (1974) 269–289, https://doi.org/10.1016/0045-7825(74)90029-2.

[17] J.B. Joshi, N.K. Nere, C.V. Rane, B.N. Murthy, C.S. Mathpati, A.W. Patwardhan, V. V. Ranade, CFD simulation of stirred tanks: comparison of turbulence models. Part I: radial flow impellers, Can. J. Chem. Eng. 89 (2011) 23–82, https://doi.org/10.1002/cjce.20446.

[18] J. Aubin, D.F. Fletcher, C. Xuereb, Modeling turbulent flow in stirred tanks with CFD: the influence of the modeling approach, turbulence model and numerical scheme, Exp. Therm. Fluid Sci. 28 (2004) 431–445, https://doi.org/10.1016/j.expthermflusci.2003.04.001.

[19] G.L. Lane, Improving the accuracy of CFD predictions of turbulence in a tank stirred by a hydrofoil impeller, Chem. Eng. Sci. 169 (2017) 188–211, https://doi.org/10.1016/j.ces.2017.03.061.

[20] L. Oshinowo, Z. Jaworski, K.N. Dyster, E. Marshall, A.W. Nienow, Predicting the tangential velocity field in stirred tanks using the multiple reference frames (MRF) model with validation by LDA measurements, 10th Eur. Conf. Mix (2000) 281–288, https://doi.org/10.1016/b978-044450476-0/50036-4.

[21] J.A. Yáñez-varela, A. Alonzo-garcia, I. González-neria, Experimental and numerical evaluation of the performance of the electrochemical reactor operated with static and dynamic electrodes in the reduction of hexavalent chromium, Chem. Eng. J. 390 (2020), 124575, https://doi.org/10.1016/j.cej.2020.124575.

[22] A. Alonzo-Garcia, V.X. Mendoza-Escamilla, S.A. Martinez-Delgadillo, I. Gonzalez-Neria, C.Del C. Gutiérrez-Torres, J.A. Jiménez-Bernal, On the performance of different rans based models to describe the turbulent flow in an agitated vessel using non-structured grids and PIV validation, Brazilian J. Chem. Eng. 36 (2019) 361–382, https://doi.org/10.1590/0104-6632.20190361s20180091.

[23] T.-H. Shih, W.W. Liou, A. Shabbir, Z. Yang, J. Zhu, A new k-ε eddy viscosity model for high reynolds number turbulent flows, Comput. Fluids 24 (1995) 227–238, https://doi.org/10.1016/0045-7930(94)00032-T.

[24] A. Iranshahi, M. Heniche, F. Bertrand, P.A. Tanguy, Numerical investigation of the mixing efficiency of the Ekato Paravisc impeller, Chem. Eng. Sci. 61 (2006) 2609–2617, https://doi.org/10.1016/j.ces.2005.11.032.

[25] M. Alliet-Gaubert, R. Sardeing, C. Xuereb, P. Hobbes, B. Letellier, P. Swaels, CFD analysis of industrial multi-staged stirred vessels, Chem. Eng. Process. Process Intensif. 45 (2006) 415–427, https://doi.org/10.1016/j.cep.2005.11.003.

[26] R. Sanjuan-galindo, M. Heniche, G. Ascanio, P.A. Tanguy, CFD Investigation of New Helical Ribbon Mixers Bottom, 2011, pp. 181–193, https://doi.org/10.1002/apj.

[27] S. Başbuğ, G. Papadakis, J.C. Vassilicos, Reduced power consumption in stirred vessels by means of fractal impellers, AIChE J. 64 (2018) 1485–1499, https://doi.org/10.1002/aic.16096.

[28] H.R. Mollinedo-Ponce-De-León, S.A. Martínez-Delgadillo, V.X. Mendoza-Escamilla, C.C. Gutiérrez-Torres, J.A. Jiménez-Bernal, Evaluation of the effect of the rotational electrode speed in an electrochemical reactor using computational fluid

dynamics (CFD) analysis, Ind. Eng. Chem. Res. 51 (2012) 5947–5952, https://doi.org/10.1021/ie201782m.
[29] M. Coroneo, G. Montante, A. Paglianti, F. Magelli, CFD prediction of fluid flow and mixing in stirred tanks: numerical issues about the RANS simulations, Comput. Chem. Eng. 35 (2011) 1959–1968, https://doi.org/10.1016/j.compchemeng.2010.12.007.
[30] R.A. Yonatan, A.G. Alejandro, M.E. Victor, G.T.C. del Carmen, J.B.J. Alfredo, M. Helvio, M.D. Sergio, Evaluation of the effect of pitched blade impellers on the performance of an electrochemical reactor, Int. J. Electrochem. Sci. 11 (2016) 9839–9854, https://doi.org/10.20964/2016.12.71.
[31] Z. Al-Qodah, M. Al-Shannag, Heavy metal ions removal from wastewater using electrocoagulation processes: A comprehensive review, Sep. Sci. Technol. 52 (2017) 2649–2676, https://doi.org/10.1080/01496395.2017.1373677.
[32] J. Bridgeman, B. Jefferson, S.A. Parsons, Computational fluid dynamics modelling of flocculation in water treatment: a review, Eng. Appl. Comput. Fluid Mech. 3 (2014) 220–241, https://doi.org/10.1080/19942060.2009.11015267.
[33] A. Bannari, C. Cirtiu, F. Kerdouss, P. Proulx, H. Ménard, Turbulence intensity in an electrochemical cell: effect on reactor performance, Chem. Eng. Process. Process Intensif. 45 (2006) 471–480, https://doi.org/10.1016/j.cep.2005.11.007.
[34] J.M. Kane, ANSYS FLUENT User's Guide, ANSYS, Inc, 2009, pp. 407–408, https://doi.org/10.1111/j.1600-0447.2011.01711.x.
[35] H. Singh, D.F. Fletcher, J.J. Nijdam, An assessment of different turbulence models for predicting flow in a baffled tank stirred with a Rushton turbine, Chem. Eng. Sci. 66 (2011) 5976–5988, https://doi.org/10.1016/j.ces.2011.08.018.
[36] V. Kolář, Vortex identification: new requirements and limitations, Int. J. Heat Fluid Flow. 28 (2007) 638–652, https://doi.org/10.1016/j.ijheatfluidflow.2007.03.004.
[37] C. Haringa, R. Vandewijer, R.F. Mudde, Inter-compartment interaction in multi-impeller mixing: part I. Experiments and multiple reference frame CFD, Chem. Eng. Res. Des. 136 (2018) 870–885, https://doi.org/10.1016/j.cherd.2018.06.005.
[38] C. Haringa, R. Vandewijer, R.F. Mudde, Inter-compartment interaction in multi-impeller mixing. Part II. Experiments, sliding mesh and large Eddy simulations, Chem. Eng. Res. Des. 136 (2018) 886–899, https://doi.org/10.1016/j.cherd.2018.06.007.